Revealing exciton-exciton couplings in semiconductors using multidimensional four-wave mixing signals

Lijun Yang and Shaul Mukamel
Chemistry Department, University of California, Irvine, California 92697-2025, USA

(Received 20 July 2007; revised manuscript received 5 November 2007; published 28 February 2008)

We show that the femtosecond four-wave mixing signal from GaAs quantum wells generated in the phase-matching direction $\mathbf{k}_1+\mathbf{k}_2-\mathbf{k}_3$ can fully resolve the pure heavy-hole, pure light-hole, and the mixed two excitons by directly observing double quantum coherences. Time-dependent Hartree-Fock contributions for different types of two excitons may be completely separated from higher-order Coulomb correlations by specific pulse polarization configurations. Simulations performed on a one-dimensional three-band tight-binding model for a GaAs quantum well are analyzed using double-sided Feynman diagrams which reveal the Liouville space pathways contributing to the various peaks.

DOI: 10.1103/PhysRevB.77.075335 PACS number(s): 78.47.−p, 78.67.De, 42.50.Md, 71.35.Cc

I. INTRODUCTION

Nonlinear four-wave mixing (FWM) experiments have long been known to provide direct probes for the many-body effects in the ultrafast dynamics of excitons in semiconductor quantum wells (SQWs).[1–13] FWM signals are commonly displayed as a function of a single (time or frequency) variable which provides a one-dimensional (1D) projection of the microscopic information. Signatures of complex many-body dynamics may not be easily identified. It is difficult to resolve the two-exciton correlations involving both heavy-hole (HH) and light-hole (LH) excitons by projecting all information into a 1D signal. During the past decade, coherent optical two-dimensional correlation spectroscopy[14–17] (2DCS) techniques have been developed and applied to many chemical, biological systems,[18–21] and SQWs.[22–26] These femtosecond analogs of nuclear magnetic resonance techniques[27,28] correlate the polarization phase evolution in independent time periods. Many-body couplings show up as cross peaks between different resonances.

2DCS signals depend on three time delays (t_1,t_2,t_3) between the incoming pulses, $\mathbf{k}_1$, $\mathbf{k}_2$, $\mathbf{k}_3$, and the signal, $\mathbf{k}_s$. Three 2DCS techniques, $S_{\mathbf{I}}$, $S_{\mathbf{II}}$, and $S_{\mathbf{III}}$ are possible for an exciton model.[15] The signals are, respectively, generated along the phase-matching directions $\mathbf{k}_{\mathbf{I}}=-\mathbf{k}_1+\mathbf{k}_2+\mathbf{k}_3$, $\mathbf{k}_{\mathbf{II}}=\mathbf{k}_1-\mathbf{k}_2+\mathbf{k}_3$, and $\mathbf{k}_{\mathbf{III}}=\mathbf{k}_1+\mathbf{k}_2-\mathbf{k}_3$. Through a Liouville space pathway analysis,[14,15,24] 2DCS can reveal detailed many-body couplings. Recent simulations of the $S_{\mathbf{I}}$ and $S_{\mathbf{II}}$ techniques show their capacity to separate coherences from different pathways and to monitor two-exciton correlations.[22–26] However, $S_{\mathbf{I}}$ and $S_{\mathbf{II}}$ only partially resolve different two-exciton resonances. Pure HH and pure LH two excitons can not be completely separated from the mixed (LH+HH) two excitons.[12,29] This was shown for $S_{\mathbf{I}}$ in Ref. 24 and for $S_{\mathbf{II}}$ in Appendix A of this paper.

Most past work on many-body interactions in SQWs had focused on the sub-HH excitons space. In a recent study of HH excitons,[32] in GaAs SQW, we demonstrated that $S_{\mathbf{III}}$ (Refs. 15, 30, and 31) is particularly sensitive to two-exciton correlations, as demonstrated recently for HH excitons in a SQW. In this work, we extend that study to include HH and LH exciton couplings. Apart from the coexistence of several types of two excitons in the LH and HH exciton couplings, two-exciton resonances are further complicated by many sources such as time-dependent Hartree-Fock (TDHF) and higher many-body correlations (HMBC) which are neglected by the TDHF.

$S_{\mathbf{III}}$, however, can completely separate pure HH, LH, and mixed two excitons. With the proper choice of pulse polarizations, it can even separate TDHF and HMBC two-exciton correlations. Moreover, as shown in Ref. 32, both frequency axes in $S_{\mathbf{III}}$ involve two excitons; one of them (t_2 or its conjugate frequency Ω_2) is solely related to two excitons and provides a very clean projection. We can thus combine the information from both axes to improve two-exciton resolution. In Sec. II, we present the model Hamiltonian and the Heisenberg equations of motion. In Sec. III, we present the level scheme for GaAs SQWs, the Feynman diagrams for $S_{\mathbf{III}}$, and the schematic 2D spectrum. Numerical calculations within and beyond TDHF are presented respectively in Secs. IV and V.

II. TIGHT-BINDING HAMILTONIAN AND EQUATIONS OF MOTION

We used a three-band one-dimensional tight-binding Hamiltonian of a linear chain with 10 sites and 40 electrons.[33–38] This model with various number of sites has been successfully employed to reproduce many experimental 1D FWM[38] and 2DCS[26] signals in GaAs SQWs.

The free band Hamiltonian is given by

$$H_K=\sum_{ijc}T_{ij}^{c}c_i^{c\dagger}c_j^{c}+\sum_{ijv}T_{ij}^{v}d_i^{v\dagger}d_j^{v}, \tag{1}$$

where $c_i^{c\dagger}$ (c_i^{c}) are the creation (annihilation) Fermi operators of electrons in site i from the conduction band c and $d_i^{v\dagger}$ (d_i^{v}) are the corresponding operators of holes in the valence band v. The diagonal elements $T_{ii}^{c,v}$ describe the site energies for the electrons (holes) in the conduction (valence) band, while the off-diagonal elements $T_{i\neq j}^{c,v}$ represent the couplings between different sites.

The optical spectrum of GaAs SQWs connects a $J=\frac{3}{2}$ valence band and a $J=\frac{1}{2}$ conduction band (the $J=\frac{1}{2}$ valence

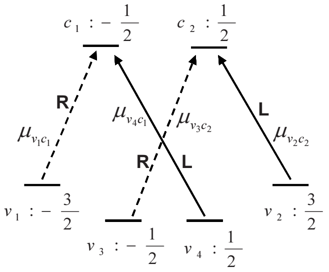

FIG. 1. Spin orbitals and selection rules for a single site of the ten-site tight-binding model.

band is well separated from the $J=\frac{3}{2}$ valence band due to spin-orbit interaction and need not be considered). Only the band edge states (Bloch vector **k** near 0) are optically active due to momentum conservation. The conduction band can thus be accurately represented by two conduction orbitals $J_z=\pm\frac{1}{2}$ and four valence orbitals, $J_z=\pm\frac{3}{2}$ (HH) and $J_z=\pm\frac{1}{2}$ (LH) states.[12,29,39,40] The dipole selection rules are presented in Fig. 1. The allowed transitions are denoted by R and L arrows, representing right and left circularly polarized photons, respectively. The corresponding transition dipoles are μ_{vc}, where $v=1,2$ denote heavy holes $\left(J_z=\pm\frac{3}{2}\right)$ and $v=3,4$ represent light holes $\left(J_z=\pm\frac{1}{2}\right)$. $c=1$ and 2 denote electrons with different spins in the conduction band $\left(J_z=\pm\frac{1}{2}\right)$.

The dipole interaction with the radiation field has the form

$$H_I=-\mathbf{E}(\mathbf{r},t)\cdot\hat{\mathbf{P}}, \tag{2}$$

where $\hat{\mathbf{P}}$ is the interband polarization operator

$$\mathbf{P}\equiv\sum_{ijvc}[\mu_{ij}^{vc}\hat{p}_{ij}^{vc}+\text{H.c.}]. \tag{3}$$

Here, μ_{ij}^{vc} are interband transition dipoles and $\hat{p}_{ij}^{vc}\equiv d_i^v c_j^c$. The electric field $\mathbf{E}(\mathbf{r},t)$ of the three incoming pulses is given by

$$\begin{aligned}\mathbf{E}(\mathbf{r},t)&=\sum_{\alpha=1}^{3}[\mathbf{E}_\alpha(\mathbf{r},t)+\mathbf{E}_\alpha^*(\mathbf{r},t)]\\&=\sum_{\alpha=1}^{3}[\mathbf{e}_\alpha\mathcal{E}_\alpha^+(t-\tau_\alpha)e^{i(\mathbf{k}_\alpha\cdot\mathbf{r}-\omega_\alpha t)}\\&\quad+\mathbf{e}_\alpha\mathcal{E}_\alpha^-(t-\tau_\alpha)e^{-i(\mathbf{k}_\alpha\cdot\mathbf{r}-\omega_\alpha t)}].\end{aligned} \tag{4}$$

Here, $\mathcal{E}_\alpha^+$ $[\mathcal{E}_\alpha^-=(\mathcal{E}_\alpha^+)^*]$ is the envelope of the positive (negative)-frequency component of the αth pulse centered at τ_α, with carrier frequency ω_α, polarization unit vector $\mathbf{e}_\alpha$, and wave vector $\mathbf{k}_\alpha$.

We next turn to the many-body couplings. We assume monopole-monopole Coulomb interaction between electrons and holes,[33,41,42]

$$H_C=\frac{1}{2}\sum_{ijcvc'v'}(c_i^{c'\dagger}c_i^{c'}-d_i^{v'\dagger}d_i^{v'})V_{ij}(c_j^{c\dagger}c_j^c-d_j^{v\dagger}d_j^v), \tag{5}$$

where

$$V_{ij}=U_0\frac{d_0}{|i-j|d_0+a_0}.$$

Here, U_0 is the interaction strength, a_0 is a spatial cutoff, and d_0 is the lattice constant.

The total Hamiltonian is finally given by

$$H=H_K+H_I+H_C. \tag{6}$$

The Heisenberg equations of motion derived from this Hamiltonian can be truncated by employing the nonlinear exciton equations (NEEs) formalism which has been widely applied to Frenkel[43,44] and Wannier[4,45,46] excitons. The optical field is treated perturbatively, while Coulomb interactions are included nonperturbatively. The NEE is most suitable for describing Coulomb correlations in the low excitation $\chi^{(3)}$ regime.[9,47,48] In this work, we focus on coherent excitations and thus only retain the two types of variables involving single exciton and two exciton, respectively.[4] To third order in the radiation field, the equations of motion for the first variable, $p_{ij}^{vc}=\langle\hat{p}_{ij}^{vc}\rangle$, are given by[34,36–38]

$$\begin{aligned}-i\frac{\partial}{\partial t}p_{ij}^{vc}-\frac{i}{t_{ex}}p_{ij}^{vc}&=-\sum_n T_{jn}^c p_{in}^{vc}-\sum_m T_{mi}^v p_{mj}^{vc}+V_{ij}p_{ij}^{vc}\\&\quad+\sum_{klv'c'}(V_{kj}-V_{ki}-V_{lj}+V_{li})\\&\quad\times[(p_{lk}^{v'c'})^*p_{lj}^{v'c}p_{ik}^{vc'}-(p_{lk}^{v'c'})^*p_{lk}^{v'c'}p_{ij}^{vc}\\&\quad-(p_{lk}^{v'c'})^*B_{lkij}^{v'c'vc}]+\mathbf{E}(\mathbf{r},t)\cdot\Bigg[(\mu_{ij}^{vc})^*\\&\quad-\sum_{klv'c'}(\mu_{il}^{vc'})^*(p_{kl}^{v'c'})^*p_{kj}^{v'c}\\&\quad+\sum_{klv'c'}(\mu_{lj}^{v'c})^*(p_{lk}^{v'c'})^*p_{ik}^{vc'}\Bigg],\end{aligned} \tag{7}$$

where the exciton dephasing time t_{ex} is introduced phenomenologically. The correlated two-exciton amplitudes $B_{lkij}^{v'c'vc}$ is defined by

$$B_{lkij}^{v'c'vc}\equiv\langle d_l^{v'}c_k^{c'}d_i^v c_j^c\rangle+\langle p_{lj}^{v'c}\rangle\langle p_{ik}^{vc'}\rangle-\langle p_{lk}^{v'c'}\rangle\langle p_{ij}^{vc}\rangle, \tag{8}$$

and satisfy the equations of motion,

$$\begin{aligned}-i\frac{\partial}{\partial t}B_{lkij}^{v'c'vc}-\frac{i}{t_{bi}}B_{lkij}^{v'c'vc}&=-\sum_m(T_{jm}^c B_{lkim}^{v'c'vc}+T_{mi}^v B_{lkmj}^{v'c^{ime}vc}\\&\quad+T_{km}^c B_{lmij}^{v'c'vc}+T_{ml}^v B_{mkij}^{v'c^{ime}vc})+(V_{lk}\\&\quad+V_{lj}+V_{ik}+V_{ij}-V_{li}-V_{kj})B_{lkij}^{v'c'vc}\\&\quad-(V_{lk}+V_{ij}-V_{li}-V_{kj})p_{ik}^{vc'}p_{lj}^{v'c}\\&\quad+(V_{ik}+V_{lj}-V_{li}-V_{kj})p_{lk}^{v'c'}p_{ij}^{vc},\end{aligned} \tag{9}$$

where t_{bi} is the two-exciton dephasing time. 2DCS signals can be calculated by selecting the spatial Fourier components of Eqs. (7) and (9) as shown in Appendix B.

In all calculations, we use the following parameters.[12,49] For the site energies and carrier coupling energies, we take $T^{c}_{i\neq j}=8$ meV, $T^{v=1,2}_{i\neq j}=4.75$ meV (HH band), and $T^{v=3,4}_{i\neq j}=2.52$ meV (LH band) to account for the in-plane dispersion of the valence-band structure in the quantum well. The site energies $T^{c}_{i=j}$ and $T^{v=1,2}_{i=j}$ are taken as half of the band gap E_g. $U_0=10$ meV and $a_0/d=0.5$. The parameters of our one-dimensional model were optimized for the description of excitons and biexcitons in quantum wells. We assumed Gaussian pulse envelopes,

$$\mathcal{E}^{\pm}_{\alpha}(t-t_{\alpha})=\exp[-(t-t_{\alpha})^{2}/\delta_{\alpha}^{2}], \tag{10}$$

where $\delta_\alpha=250$ fs for the calculations of all 2DCS signals and $\delta_\alpha=100$ fs for linear absorption. The carrier frequency was detuned by $\Delta\omega_\alpha=3.62$ meV to the blue of the HH exciton energy.

III. $S_{\mathbf{III}}$ TECHNIQUE APPLIED TO GaAs QUANTUM WELLS

To investigate the excitonic structure of our model [Eq. (6)], we transform from the real (site) space to momentum k space. Applying periodic boundary conditions gives the following k values:[38]

$$k=0,\ \pm\frac{2\pi}{Na},\ \pm\frac{4\pi}{Na},\ \ldots,\ \pm\frac{(N/2-1)2\pi}{Na},\ \frac{\pi}{a},$$

where N is the number of sites. For $N=10$, there are 10 HH and 10 LH single exciton states. However, because $\pm k$ are degenerate, we have 12 different energies. We first calculate the linear absorption $\alpha(\omega)$ using[14,24]

$$\alpha(\omega)=\frac{\omega_j}{n' c\epsilon_0}\,\mathrm{Im}\left[\frac{\mathbf{P}(\omega)\cdot\mathbf{E}^{*}_{\mathrm{opt}}(\omega)}{|\mathbf{E}_{\mathrm{opt}}(\omega)|^{2}}\right], \tag{11}$$

where n' is the average, frequency-independent refractive index of the quantum well, ϵ_0 is the vacuum permittivity, and c is the speed of light. $\mathbf{E}_{\mathrm{opt}}(\omega)$ is Fourier transform of the pulse envelope $\mathcal{E}^{+}_{\alpha}$. $\mathbf{P}(\omega)$ is the Fourier transform of the linear polarization obtained by integrating the linear equation [Eq. (B5)] over a time period of 38 ps with 1660 time grid points.

Figure 2 shows the calculated linear absorption. There are six pairs of peaks (one pair is very weak) and each pair corresponds to HH and LH band contributions. The small negative features in the absorption reflect numerical error. The two strong peaks to the red are, respectively, referred to as HH and LH excitons. These are the dominant peaks in the linear or nonlinear responses of a quantum well. As N increases, the strength of other peaks will be reduced and their contributions to the linear absorption will form a continuum. In the numerical calculations, we used spectrally narrow pulses to reduce the influence of continuum states. Thus, in the following analysis, we shall only consider the two marked HH and LH excitons.

The many-electron level scheme[12,29,39,40] including HH and LH excitons and four bound two-exciton transitions is presented in Fig. 3. The ground state to exciton dipoles (superpositions of μ_{vc}) and the exciton to two-exciton dipoles are collectively denoted by μ_{ge} and μ_{ef}, respectively. Subscripts g, e, and f represent, respectively, the ground state, the single, and the two-exciton manifold. e can be either $e_H(e'_H)$ or $e_L(e'_L)$ denoting HH and LH excitons. f can be either f_H, f_L, or f_M representing, respectively, HH, LH, and mixed two excitons. The unbound two-exciton transitions (not shown for clarity) will be included in the numerical calculations.

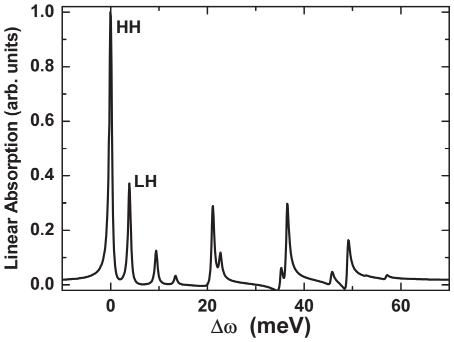

FIG. 2. Linear Absorption of the ten-site chain model for a semiconductor quantum well. Δω=0 is the HH exciton energy which is around 1.5 eV (it varies for different samples).

We shall consider the 2D projection of the $S_{\mathbf{III}}(t_3,t_2,t_1)$ signal[24] in the (Ω_3,Ω_2) plane for fixed t_1,

$$S_{\mathbf{III}}(\Omega_3,\Omega_2,t_1)\equiv\int\int dt_3dt_2S_{\mathbf{III}}(t_3,t_2,t_1)e^{i\Omega_3t_3}e^{i\Omega_2t_2}. \tag{12}$$

Within the rotating wave approximation, two basic Feynman diagrams (vii) and (viii) (in the notation of Refs. 15 and 24) contribute to this signal, each gives six diagrams, as shown in Fig. 4, when all contributions of HH and LH transitions are spelled out. The contributions of each diagram (Liouville space pathway) to the signal are represented by different symbols shown at the bottom. Solid (open) symbols denote redshifted (blueshifted) two excitons. Open circles describe the contributions from bare two excitons whose contributions vary for f_H, f_L, and f_M. However, we denote them collectively by the same symbol (circle) for clarity.

With the help of Fig. 4, we can schematically sketch the $S_{\mathbf{III}}$ spectrum. This is shown in Fig. 5, where the overlapping symbols are slightly displaced for clarity. We first consider

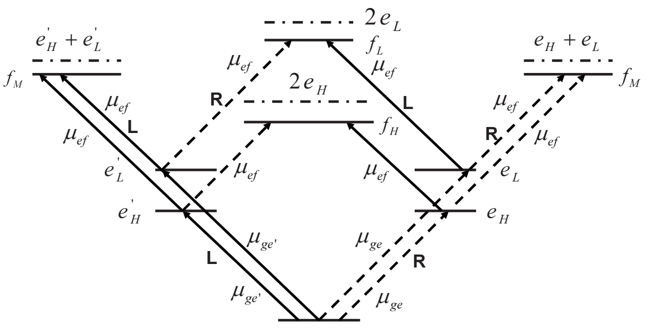

FIG. 3. Exciton level scheme for GaAs semiconductors.

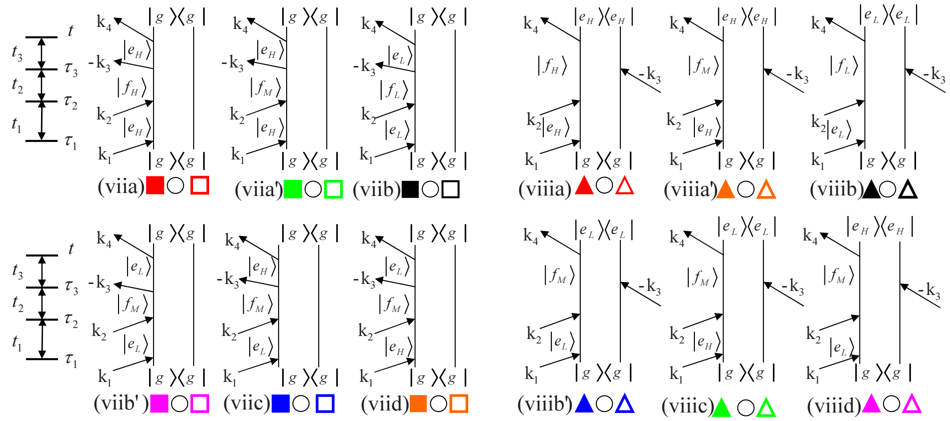

FIG. 4. (Color online) Feynman diagrams for S_{III} technique derived from diagrams (vii) and (viii) of Fig. 1 in Ref. 24.

the HH exciton contributions [diagrams (viia) and (viiia)]. Diagram (viiia), when f_H is redshifted and equals to $2e_H - \Delta_{H_1}$, shows the resonance between $2e_H - \Delta_{H_1}$ and the ground state during the t_2 period. During t_3, (viiia) shows a resonance between $f_H = 2e_H - \Delta_{H_1}$ and e_H with frequency $e_H - \Delta_{H_1}$. Therefore, according to (viiia) and taking $f_H = 2e_H - \Delta_{H_1}$, we have a peak at $(\Omega_3, \Omega_2) = (e_H - \Delta_{H_1}, 2e_H - \Delta_{H_1})$ (solid red triangle). The two coordinates correspond, respectively, to the resonance energies during the evolution time periods t_3 and t_2. The blueshifted two-exciton energy $f_H = 2e_H + \Delta_{H_2}$ in (viiia) gives a peak at $(\Omega_3, \Omega_2) = (e_H + \Delta_{H_2}, 2e_H + \Delta_{H_2})$ (open red triangle). Similarly, using diagram (viia) and by taking, respectively, $f_H = 2e_H - \Delta_{H_1}$ and $2e_H + \Delta_{H_2}$, we obtain the solid and open red squares. For bare two excitons, $f_H = 2e_H$, there are no HMBC two-exciton coupling[50] and both diagrams (viia) and (viiia) contribute to the signal at $(e_H, 2e_H)$ (open circle). Finally, the analysis of other diagrams involving LH excitons is similar to the case with only HH excitons.

The unique capacity of S_{III} to resolve two excitons within the HH region have been demonstrated in Ref. 32. The Ω_2 axis provides a clean projection of two excitons which only contains two exciton to ground state resonances. By combining the two-exciton information along the Ω_2 and Ω_3 axes, we can achieve high resolution. We note that the peaks related only to HH two excitons around $(\Omega_3, \Omega_2) = (e_H, 2e_H)$ and the LH two excitons around $(e_L, 2e_L)$ are separated from the mixed two-exciton peaks at $\Omega_2 = e_H + e_L$. Thus, the mixed two excitons do not affect the pure HH (LH) two excitons, as is the case in $\mathbf{S}_{\text{I}}$ (Ref. 24) and $\mathbf{S}_{\text{II}}$ (see Appendix A) techniques. Moreover, as we shall show later, by choosing specific pulse polarizations, S_{III} can also fully separate the correlated pure or mixed two excitons from their corresponding TDHF contributions. For example, in the vicinity of $(e_H, 2e_H)$, there will be only contributions from HMBC but no bare two excitons arising from TDHF.

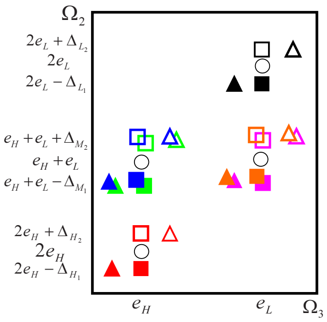

FIG. 5. (Color online) The $\mathbf{S}_{\text{III}}(\Omega_3, \Omega_2, t_1)$ signal derived from Fig. 4.

IV. TIME-DEPENDENT HARTREE-FOCK SIMULATIONS OF TWO-DIMENSIONAL CORRELATION SPECTROSCOPY

$\mathbf{S}_{\text{III}}$ is equal to $\mathbf{P}^{[\mathbf{k}_{\text{III}}]}(t_3, t_2, t_1, t)$, where $\mathbf{P}^{[\mathbf{k}_{\text{III}}]}$ is the interband polarization in the phase-matching direction $\mathbf{k}_{\text{III}}$, given by

$$\mathbf{P}^{[\mathbf{k}_{\text{III}}]}(t_3, t_2, t_1, t) \equiv \sum_{ijvc} \mu_{ij}^{vc} p_{ij}^{vc:[\mathbf{k}_{\text{III}}]}(t_3, t_2, t_1, t). \tag{13}$$

To calculate the 2D spectra, we first compute $\mathbf{P}^{[\mathbf{k}_{\text{III}}]}$ for fixed $t_1 = 150$ fs from $t_3 = 0$ to 28 ps with 660 time grid points by solving Eqs. (B1), (B5), and (B6). These calculations were then repeated by varying t_2 from $\overline{t}_2 = 0$ ps to 14 ps on a 330-point grid.

We first present calculations at the TDHF level. To that end, we set the correlated two-exciton variables $B_{lkij}^{v'c'vc:\mathbf{k}_1+\mathbf{k}_2}$ in Eq. (B1) to be zero. According to Eq. (8), this is equivalent to the following TDHF decoupling:

$$\begin{aligned}\langle d_l^{v'} c_k^{c'} d_i^{v} c_j^{c} \rangle &= p_{lk}^{v'c'} p_{ij}^{vc} - p_{lj}^{v'c} p_{ik}^{vc'} \\ &= \langle d_l^{v'} c_k^{c'} \rangle \langle d_i^{v} c_j^{c} \rangle - \langle d_l^{v'} c_j^{c} \rangle \langle d_i^{v} c_k^{c'} \rangle. \end{aligned} \tag{14}$$

Using the parameters given in Sec. II, we obtained the 2D spectra [Eq. (12)] shown in Fig. 6. In all figures, the origin is e_H for Ω_3 and $2e_H$ for Ω_2. For XRRR polarization configuration (indices are chronologically ordered from right to left, i.e., $\mathbf{k}_1$ is R and signal is X), only pure HH two excitons appear at (0,0) and pure LH two excitons appear at around (4, 8), as shown in the top panel. For the XRLR configuration (middle panel), only mixed two excitons appear at (0,4) and (4,4). All possible two excitons are seen for XXXX configuration (bottom panel). Finally, we note that only bare two excitons show up at this TDHF level.[50]

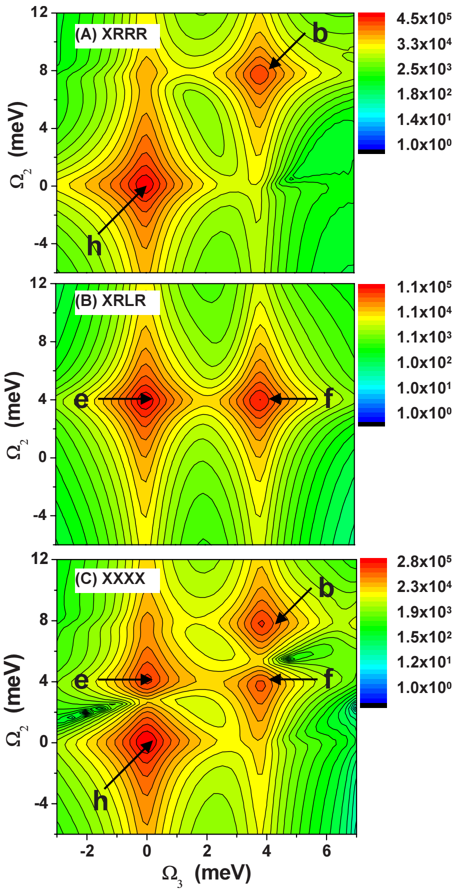

FIG. 6. (Color online) Calculated $\mathbf{S}_{\mathbf{III}}(\Omega_3,\Omega_2,t_1)$ using various pulse polarization configurations at the TDHF level. $\Omega_3=0$ corresponds to HH exciton energy e_H and $\Omega_2=0$ to $2e_H$. $t_1=150$ fs and $\bar{t}_2=0$ fs.

Figure 6 can be interpreted using the wave-vector-selected equations of motion in Appendix B. In Eq. (B1), apart from the term $-\mathcal{S}_{\mathbf{k}_3\mathbf{k}_2\mathbf{k}_1}(p_{lk}^{v'c':\mathbf{k}_3})^* B_{lkij}^{v'c'vc:\mathbf{k}_1+\mathbf{k}_2}$ containing the correlated two excitons, all other terms are within TDHF. The permutation symbol $\mathcal{S}_{\mathbf{k}_3\mathbf{k}_2\mathbf{k}_1}$ and its action on different expressions are defined in Eqs. (B2) and (B4) in Appendix B. Among the TDHF terms, the terms containing optical field $\mathbf{E}_\alpha(t)$ $(\alpha=1,2,3)$ represent Pauli blocking. Our simulations show that their contributions to the signal are very small. Another nonlinear TDHF term $\mathcal{S}_{\mathbf{k}_3\mathbf{k}_2\mathbf{k}_1}(p_{lk}^{v'c':\mathbf{k}_3})^* p_{lk}^{v'c':\mathbf{k}_2} p_{ij}^{vc:\mathbf{k}_1}$ in Eq. (B1) does not contribute to the signal for translationally invariant systems.[38] Retaining only the dominant TDHF term $\mathcal{S}_{\mathbf{k}_3\mathbf{k}_2\mathbf{k}_1}(p_{lk}^{v'c':\mathbf{k}_3})^* p_{lj}^{v'c:\mathbf{k}_2} p_{ik}^{vc':\mathbf{k}_1}$, Eq. (B1) becomes

$$-i\frac{\partial}{\partial t}p_{ij}^{vc:[\mathbf{k}_1+\mathbf{k}_2-\mathbf{k}_3]} \sim \sum_{klv'c'} [\mathcal{S}_{\mathbf{k}_3\mathbf{k}_2\mathbf{k}_1}(p_{lk}^{v'c':\mathbf{k}_3})^* p_{lj}^{v'c:\mathbf{k}_2} p_{ik}^{vc':\mathbf{k}_1}]. \tag{15}$$

R polarized photons can induce two transitions, (v_1,c_1) and (v_3,c_2). L polarized photons induce two other transitions, (v_2,c_2) and (v_4,c_1), as shown in Fig. 1. We first consider the term $(p_{lk}^{v'c':\mathbf{k}_3})^* p_{lj}^{v'c:\mathbf{k}_2} p_{ik}^{vc':\mathbf{k}_1}$ in Eq. (15) arising from one permutation of $\mathcal{S}_{\mathbf{k}_3\mathbf{k}_2\mathbf{k}_1}$.

For the XRRR configuration, the indices (v',c') in $(p_{lk}^{v'c':\mathbf{k}_3})^*$ can be either (v_1,c_1) or (v_3,c_2) for the R polarized pulse $\mathbf{k}_3$, as shown in Fig. 1. For $(v',c')=(v_1,c_1)$, we have

$$\sum_{klv'c'} (p_{lk}^{v'c':\mathbf{k}_3})^* p_{lj}^{v'c:\mathbf{k}_2} p_{ik}^{vc':\mathbf{k}_1} = \sum_{kl} (p_{lk}^{v_1c_1:\mathbf{k}_3})^* p_{lj}^{v_1c:\mathbf{k}_2} p_{ik}^{vc_1:\mathbf{k}_1}. \tag{16}$$

Since both pulses $\mathbf{k}_2$ and $\mathbf{k}_1$ are R polarized, the c and v indices in Eq. (16) can only assume, respectively, the values $c=c_1$ and $v=v_1$. Therefore, in this case, we have only pure HH two excitons. Similarly, if the indices (v',c') in $(p_{lk}^{v'c':\mathbf{k}_3})^*$ take the other possible value of (v_3,c_2), then we only have pure LH two excitons because pulses $\mathbf{k}_2$ and $\mathbf{k}_1$ can only excite LH excitons through transitions (v_3,c_2). Analysis of other terms arising from the permutation of $\mathcal{S}_{\mathbf{k}_3\mathbf{k}_2\mathbf{k}_1}$ yields the same conclusion: XRRR can only access pure HH or LH two excitons at the TDHF level. Mixed two excitons are not excited.

For the XRLR configuration, we consider the same TDHF term $(p_{lk}^{v'c':\mathbf{k}_3})^* p_{lj}^{v'c:\mathbf{k}_2} p_{ik}^{vc':\mathbf{k}_1}$ in Eq. (15) where the R polarized pulse $\mathbf{k}_3$ leads to $(v',c')=(v_1,c_1)$ or (v_3,c_2) in $(p_{lk}^{v'c':\mathbf{k}_3})^*$. For $(v',c')=(v_1,c_1)$, we again obtain Eq. (16). Because pulse $\mathbf{k}_2$ is L polarized, $p_{lj}^{v_1c:\mathbf{k}_2}$ in Eq. (16) is always zero for any c values. Even $c=c_1$, $p_{lj}^{v_1c:\mathbf{k}_2}=p_{lj}^{v_1c_1:\mathbf{k}_2}$ is still zero because L polarized photons cannot access (v_1,c_1) transition, as shown in Fig. 1. Thus, the TDHF term $(p_{lk}^{v'c':\mathbf{k}_3})^* p_{lj}^{v'c:\mathbf{k}_2} p_{ik}^{vc':\mathbf{k}_1}$ does not contribute to the signal when $(v',c')=(v_1,c_1)$.

We next consider other terms arising from the permutations of $(p_{lk}^{v'c':\mathbf{k}_3})^* p_{lj}^{v'c:\mathbf{k}_2} p_{ik}^{vc':\mathbf{k}_1}$. Under the same condition $(v',c')=(v_1,c_1)$, we have

$$\begin{aligned}\mathcal{S}_{\mathbf{k}_3\mathbf{k}_2\mathbf{k}_1} \sum_{klv'c'} (p_{lk}^{v'c':\mathbf{k}_3})^* p_{lj}^{v'c:\mathbf{k}_2} p_{ik}^{vc':\mathbf{k}_1} \\ = \sum_{klv'c'} (p_{lk}^{v'c':\mathbf{k}_3})^* p_{lj}^{v'c:\mathbf{k}_1} p_{ik}^{vc':\mathbf{k}_2} + \cdots \\ = \sum_{kl'} (p_{lk}^{v_1c_1:\mathbf{k}_3})^* p_{lj}^{v_1c:\mathbf{k}_1} p_{ik}^{vc_1:\mathbf{k}_2} + \cdots .\end{aligned} \tag{17}$$

Equation (17) can contribute to the FWM signal by taking $c=c_1$ and $v=v_4$, which gives

$$-i\frac{\partial}{\partial t}p_{ij}^{vc:[\mathbf{k}_1+\mathbf{k}_2-\mathbf{k}_3]} \sim \sum_{kl'} (p_{lk}^{v_1c_1:\mathbf{k}_3})^* p_{lj}^{v_1c_1:\mathbf{k}_1} p_{ik}^{v_4c_1:\mathbf{k}_2} + \cdots , \tag{18}$$

where R polarized pulse $\mathbf{k}_1$ accesses (v_1,c_1) transition and L polarized pulse $\mathbf{k}_2$ accesses (v_4,c_1) transition, which are both possible, as shown in Fig. 1. Moreover, when $c=c_1$ and $v=v_4$, $p_{ij}^{vc:[\mathbf{k}_1+\mathbf{k}_2-\mathbf{k}_3]}$ becomes $p_{ij}^{v_4c_1:[\mathbf{k}_1+\mathbf{k}_2-\mathbf{k}_3]}$ and is also accessible by the final X polarized heterodyne pulse according to the selection rules. Thus, in Eq. (18), pulses $\mathbf{k}_1$ and $\mathbf{k}_2$, respectively, create a HH exciton and a LH exciton, thus forming mixed two excitons, as shown in Fig. 6(B). The same conclusion holds if the indices (v',c') in $(p_{lk}^{v'c':\mathbf{k}_3})^*$ assume the other possible value of (v_3,c_2). The above analysis explains why only mixed two excitons are created by the XRLR configuration at the TDHF level.

Finally, the XXXX configuration involves a superposition of both XRRR and XRLR and is thus nonselective. Both pure HH (LH) two excitons and mixed two excitons are generated, as shown in Fig. 6(C).

V. HIGHER CORRELATION EFFECTS: BEYOND TIME-DEPENDENT HARTREE-FOCK

The full NEE calculation, beyond TDHF, reveals many-body correlations among HH and LH excitons. By selecting pulse polarizations, one can completely separate correlation effects from TDHF contributions for different types of two excitons. For the XRRR configuration [Fig. 6(A)], any peaks other than (b) and (h) would be due to HMBC. For example, peaks around (0, 4) and (4, 4) must be from the correlated mixed two excitons. This is because around these positions there should be no TDHF contributions according to Fig. 6(A) but there should be HMBC contributions from mixed two excitons according to Fig. 5. For XRLR [Fig. 6(B)], all peaks other than (e) and (f) are induced by HMBC. For example, the peaks around (0, 0) and (4, 8) must be from the correlated pure HH (LH) two excitons. This is because there are no TDHF contributions in their vicinity according to Fig. 6(B). However, there should be contributions from correlated pure HH two excitons at (0, 0) and pure LH two excitons at (4, 8) according to Fig. 5. Thus, the XRRR and XRLR configurations completely separate the correlation effects from the TDHF contributions for mixed two excitons and pure HH (LH) two excitons.

In Fig. 7, we present the full NEE calculation for the XRLR configuration. To show how 2D spectra evolve with time-delay parameters, in panels A and B, we use different values of t_1 and the initial t_2, $\bar{t}_2$. We see new peaks [(a) and (g)] not predicted in Fig. 5. The origin of these peaks is not clear. It may be due to interferences along different axes, or among LH and HH excitons arising from small LH and HH exciton splitting. For example, peak (a) in panel A might be the tail of peak (e) along Ω_2 but may become an isolated peak due to the interference with LH excitons along Ω_3. However, it is easy to identify peaks such as (a) and (g) in the 2D spectra because their Ω_2 values vary with different excitation conditions. Thus, we can easily exclude them when determining the two-exciton correlation energy. Using Fig. 7(A), we can directly deduce the bound correlation energies for various two excitons. From peaks [(c) and (d)] and [(m) and (n)], we obtain that the two-exciton binding energies for HH and LH two excitons are, respectively, 1.35 and 1.45 meV.

The peaks that follow the predicted pattern in Fig. 5 such as (b)–(f), (h), (m), and (n) in panels (A) and (B) retain the same Ω_2 values for different time-delay parameters or pulse polarization configurations. Therefore, these peaks can be used to determine two-exciton couplings, attractive two-exciton binding energy (TBE) or repulsive two-exciton scattering energy (TSE). To that end, we need only identify the peaks below and above the lines $\Omega_2=2e_H=0, e_H+e_L \simeq 4$ meV and $2e_L \simeq 8$ meV, respectively. For example, we can obtain the energy of peak (c) along Ω_2 and thus get the TBE for LH two excitons. Note that the unresolved peak, a shoulder (d), to the red of peak (c), as predicted by Fig. 5. Peaks (d) and (c) always appear in pairs and thus can help identify both peaks even though they are very weak and not well resolved. Similarly, we obtain the TBE for HH two excitons from peaks (m) and (n). Moreover, by using spectrally narrow pulses and different detunings, one can even clearly show the blueshifted TSE of correlated same-spin excitons.[32] For current pulse parameters, the TSE feature is not seen.

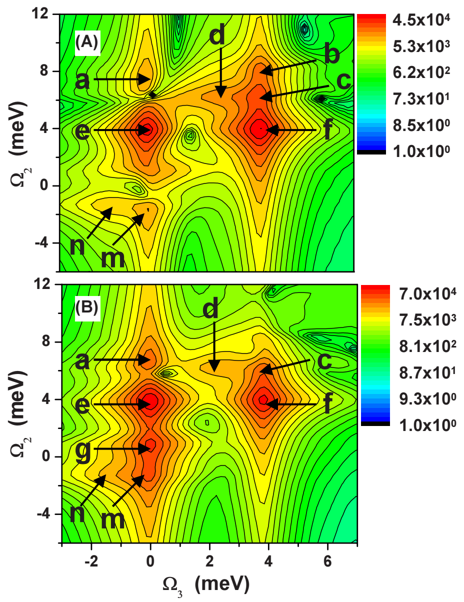

FIG. 7. (Color online) Calculated $\mathbf{S_{III}}(\Omega_3,\Omega_2,t_1)$ spectra with XRLR polarization configuration. Exciton correlations are included [Eqs. (7) and (9)]. (A) t_1=300 fs and $\bar{t}_2$=300 fs. (B) t_1=150 fs and $\bar{t}_2$=0 fs.

The spectra shown in Fig. 7 completely separate the pure HH(LH) two excitons from mixed two excitons [peaks (e) and (f)]. We can thus accurately determine the correlation energies of pure HH and LH two-excitons, even when the two-exciton features are weak [e.g., peaks (m) and (n) in Fig. 7(A)]. The XRLR configuration excludes the TDHF contributions at (0, 0) and (4, 8) which contain correlated HH (LH) two excitons and thus further enhance the resolution. Such resolution may not be achieved by other techniques ($\mathbf{S_I}$ and $\mathbf{S_{II}}$) where features such as (d) and (c) or (m) and (n) are hidden under the stronger mixed two-exciton peaks, (e) and (f).

To check the convergence of the correlation energies, we have repeated the calculation of the 2D spectrum with the same parameters as in Fig. 7(A) but with different basis sets. These are shown in Figs. 8(A) (14 sites) and 8(B) (20 sites). We note that the main features such as mixed exciton peaks (e) and (f), pure LH two-exciton peaks (c) and (d), and pure HH two-exciton peaks (m) and (n) had converged and agree with Fig. 7(A). In fact, the binding energies of pure HH and

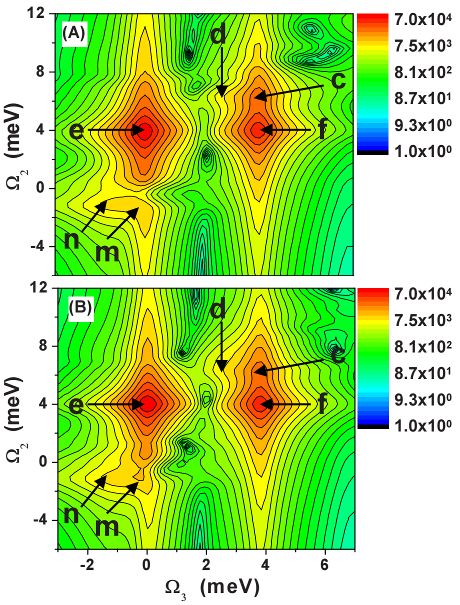

FIG. 8. (Color online) Calculated $\mathbf{S}_{\mathbf{III}}(\Omega_3,\Omega_2,t_1)$ spectra with same parameters as in Fig. 7(A) but with different basis size: (A) 14 sites and (B) 20 sites.

LH two excitons can be obtained with very high resolution in this experiment. For example, although we cannot resolve clearly peaks (c) and (d), by connecting the ridges between peaks (c) and (d), we can obtain a straight line, whose energy along Ω_2 accurately gives the LH two-exciton binding energy. However, we also note that the XRLR polarization configuration does not resolve the correlated mixed two excitons because peaks (e) and (f) are dominated by the TDHF contribution, as shown in Fig. 6(B). The contributions from HMBC mixed two excitons will overlap with these TDHF contributions and may not be easily distinguished.

The XRRR spectra are shown in Fig. 9. As in Fig. 7, the origin of peaks (a) and (g) is not clear and might be attributed to the cross interferences among HH and LH excitons along different axes. They do not follow the pattern in Fig. 5 and their Ω_2 values vary for different configurations. According to Fig. 6(A), there should be no signals at positions (e) and (f) for the XRRR configuration at the TDHF level. Therefore, (e) and (f) in Fig. 9 must come from correlated mixed two excitons, according to Fig. 5. In this way, we achieve a complete separation of correlated mixed two excitons from their TDHF counterparts. In other techniques, $\mathbf{S}_{\mathbf{I}}$ (Ref. 24) and $\mathbf{S}_{\mathbf{II}}$ (Appendix A), correlated mixed two excitons always overlap with other dominant peaks and may not be easily resolved. Furthermore, we note that the mixed two excitons formed by two same-spin excitons do not have appreciable red shifts or blueshifts from $e_H+e_L\simeq4$ meV. This indicates that if using other techniques these correlation features will completely overlap with the stronger single-exciton transitions and may not be detected at all.

The XXXX spectra are shown in Fig. 10. As expected, this configuration cannot completely separate the correlation and TDHF contributions neither for pure HH (LH) two excitons nor for mixed two excitons. This is because the TDHF peaks occupy all the major peak positions, as shown in Fig. 6(C). Panels (A) and (B) are calculated with the same parameters except that t_1 and the initial t_2, $\bar{t}_2$, are slightly different. We find strong interferences between the within and beyond TDHF contributions. For example, even though peaks (e) and (f) in Fig. 6(C) show the mixed two excitons from TDHF contributions, in Fig. 10, peak (f) is missing due to interference. However, we can still resolve several peaks such as (b), (e), and (h) which have the same Ω_2 values as compared to the corresponding peaks in Figs. 7 and 9.

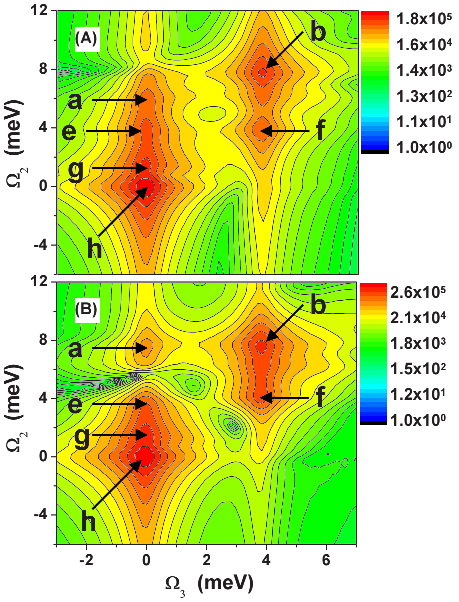

FIG. 9. (Color online) Calculated $\mathbf{S}_{\mathbf{III}}(\Omega_3,\Omega_2,t_1)$ spectra with XRRR polarization configuration. Exciton correlations are included [Eqs. (7) and (9)]. (A) $t_1=300$ fs and $\bar{t}_2=300$ fs. (B) $t_1=150$ fs and $\bar{t}_2=0$ fs.

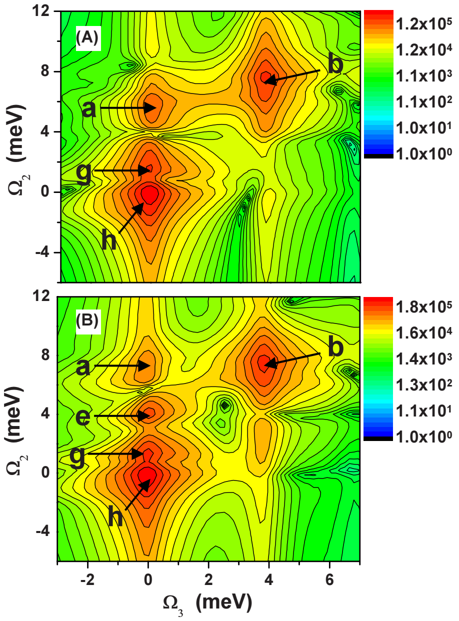

FIG. 10. (Color online) Calculated $\mathbf{S}_{\mathbf{III}}(\Omega_3,\Omega_2,t_1)$ spectra with XXXX polarization configuration. (A) $t_1=300$ fs and $\bar{t}_2=300$ fs. (B) $t_1=150$ fs and $\bar{t}_2=0$ fs.

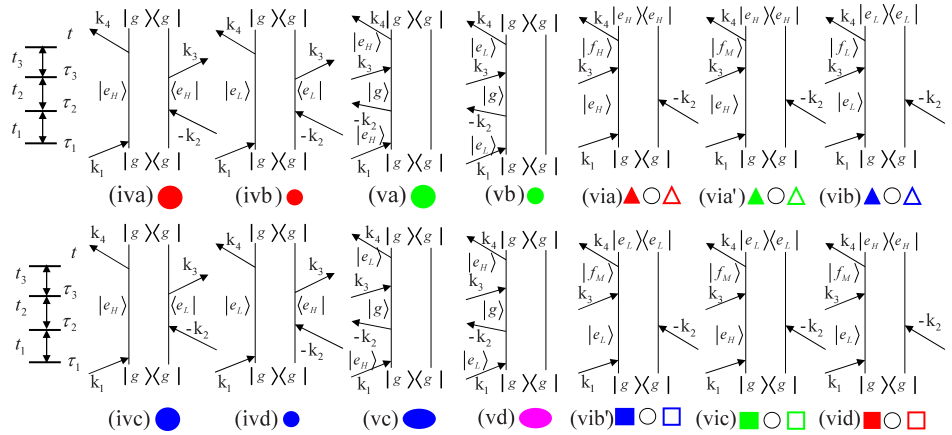

FIG. 11. (Color online) Feynman diagrams for $S_{\mathbf{II}}$ technique derived from diagrams (iv), (v), and (vi) of Fig. 1 in Ref. 24.

In summary, the proposed 2DCS technique is particularly useful for resolving different correlated two excitons. The separation of two-exciton HMBC effects from the TDHF level may be achieved by selecting specific pulse polarizations.

ACKNOWLEDGMENT

The support of the Chemical Sciences, Geosciences, and Biosciences Division, Office of Basic Energy Sciences, U.S. Department of Energy is gratefully acknowledged.

APPENDIX A: THE $S_{\mathbf{II}}$ TECHNIQUE

The $S_{\mathbf{I}}$ technique was analyzed in Ref. 24. For completeness and comparison with the $S_{\mathbf{III}}$ technique discussed in this work, we present below a Feynman diagram analysis of the $S_{\mathbf{II}}$ technique. We denote the heterodyne-detected signal generated by three very short (impulsive) pulses along the phase-matching direction $\mathbf{k}_{\mathbf{II}}=\mathbf{k}_1-\mathbf{k}_2+\mathbf{k}_3$ as $S_{\mathbf{II}}(t_3,t_2,t_1)$.[24] The corresponding 2D signal defined as

$$S_{\mathbf{II}}(\Omega_3,t_2,\Omega_1) \equiv \int\int dt_3 dt_1 S_{\mathbf{II}}(t_3,t_2,t_1) e^{i\Omega_3 t_3} e^{i\Omega_1 t_1} \tag{A1}$$

will be displayed in the (Ω_3,Ω_1) plane for a fixed t_2. Using the notation of Refs. 15 and 24, this signal is described by three basic Feynman diagrams (iv), (v), and (vi), where (iv) and (v) only involve single excitons and (vi) involves both single and two excitons. The complete set of diagrams derived from the three basic diagrams by specifying the various HH and LH excitons are shown in Fig. 11. f_H, f_L, and f_M denote the various two excitons. For example, due to Coulomb interactions, f_H can be either redshifted $f_H=2e_H-\Delta_{H_1}$, bare $f_H=2e_H$, or blueshifted $f_H=2e_H+\Delta_{H_2}$ compared to twice the single HH exciton energy, $2e_H$. In diagrams (via) to (vid), each solid symbol describes a type of redshifted two excitons and the corresponding open symbol describes blueshifted ones. Open circles denote contributions from bare two excitons.

The $S_{\mathbf{II}}$ signals from (iva)–(ivd), (va)–(vd), and (via)–(vid) are plotted schematically in Figs. 12(iv), 12(v), and 12(vi), respectively. The total spectrum obtained by summing all diagrams is shown in the panel (s) of Fig. 12, where overlapping peaks are slightly displaced for clarity.

Note that different types of two excitons are only partially separated in panel (s). Pure HH (LH) two excitons (e.g., solid red triangle) are still overlapped with the mixed two excitons (e.g., solid green square). The situation is similar in all other 2D projections of $\mathbf{S}_{\mathbf{II}}$ where pure HH (LH) two excitons and the mixed two excitons may not be fully separated.

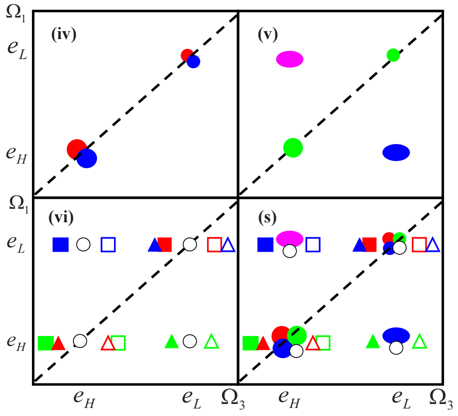

FIG. 12. (Color online) The $S_{\mathbf{II}}(\Omega_3,t_2,\Omega_1)$ signal. (iv) Contributions of pathways (iva), (ivb), (ivc), and (ivd). (v) Contributions of pathways (va), (vb), (vc), and (vd). (vi) Contributions of pathways (via) to (vid). (x) Total spectrum. The dashed line marks the diagonal peaks.

APPENDIX B: WAVE-VECTOR SELECTION FOR THE S_{III} TECHNIQUE

In our earlier work,[24] we presented the equations of motion for calculating $S_{\mathbf{I}}$ 2DCS for a two-pulse configuration. Below, we extend them to calculate $S_{\mathbf{III}}$ 2DCS signals induced by three pulses. To that end, we present the equations of motion for selecting the $\mathbf{k}_{\mathbf{III}}=\mathbf{k}_1+\mathbf{k}_2-\mathbf{k}_3$ component of the interband density matrix p_{ij}^{vc} in Eq. (7). Additional terms and equations are necessary in the three-pulse scheme due to the more permutations among different pulses.

$$
\begin{aligned}
-i\frac{\partial}{\partial t}p_{ij}^{vc:[\mathbf{k}_1+\mathbf{k}_2-\mathbf{k}_3]}-\frac{i}{\tau_{ex}}p_{ij}^{vc:[\mathbf{k}_1+\mathbf{k}_2-\mathbf{k}_3]} ={}& -\sum_n T_{jn}^{c}p_{in}^{vc:[\mathbf{k}_1+\mathbf{k}_2-\mathbf{k}_3]}-\sum_m T_{mi}^{v}p_{mj}^{vc:[\mathbf{k}_1+\mathbf{k}_2-\mathbf{k}_3]}+V_{ij}p_{ij}^{vc:[\mathbf{k}_1+\mathbf{k}_2-\mathbf{k}_3]}+\sum_{klv'c'}(V_{kj}-V_{ki}-V_{lj}+V_{li})\\
&\cdot[\mathcal{S}_{\mathbf{k}_3\mathbf{k}_2\mathbf{k}_1}(p_{lk}^{v'c':\mathbf{k}_3})^{*}p_{lj}^{v'c:\mathbf{k}_2}p_{ik}^{vc':\mathbf{k}_1}-\mathcal{S}_{\mathbf{k}_3\mathbf{k}_2\mathbf{k}_1}(p_{lk}^{v'c':\mathbf{k}_3})^{*}p_{lk}^{v'c':\mathbf{k}_2}p_{ij}^{vc:\mathbf{k}_1}\\
&-\mathcal{S}_{\mathbf{k}_3\mathbf{k}_2\mathbf{k}_1}(p_{lk}^{v'c':\mathbf{k}_3})^{*}B_{lkij}^{v'c'vc:\mathbf{k}_1+\mathbf{k}_2}]-\mathbf{E}_3^{*}(t)\cdot\sum_{klv'c'}[(\mu_{il}^{vc'})^{*}\mathcal{S}_{\mathbf{k}_2\mathbf{k}_1}p_{kl}^{v'c':\mathbf{k}_2}p_{kj}^{v'c:\mathbf{k}_1}\\
&+(\mu_{lj}^{v'c})^{*}\mathcal{S}_{\mathbf{k}_2\mathbf{k}_1}p_{lk}^{v'c':\mathbf{k}_2}p_{ik}^{vc':\mathbf{k}_1}]-\mathbf{E}_2(t)\cdot\sum_{klv'c'}[(\mu_{il}^{vc'})^{*}\mathcal{S}_{\mathbf{k}_3\mathbf{k}_1}(p_{kl}^{v'c':\mathbf{k}_3})^{*}p_{kj}^{v'c:\mathbf{k}_1}\\
&+(\mu_{lj}^{v'c})^{*}\mathcal{S}_{\mathbf{k}_3\mathbf{k}_1}(p_{lk}^{v'c':\mathbf{k}_3})^{*}p_{ik}^{vc':\mathbf{k}_1}]-\mathbf{E}_1(t)\cdot\sum_{klv'c'}[(\mu_{il}^{vc'})^{*}\mathcal{S}_{\mathbf{k}_3\mathbf{k}_2}(p_{kl}^{v'c':\mathbf{k}_3})^{*}p_{kj}^{v'c:\mathbf{k}_2}\\
&+(\mu_{lj}^{v'c})^{*}\mathcal{S}_{\mathbf{k}_3\mathbf{k}_2}(p_{lk}^{v'c':\mathbf{k}_3})^{*}p_{ik}^{vc':\mathbf{k}_2}],
\end{aligned}
\tag{B1}
$$

where τ_{ex} describes exciton dephasing time. In Eq. (B1), $\mathcal{S}_{\mathbf{k}_i\mathbf{k}_j}$ and $\mathcal{S}_{\mathbf{k}_i\mathbf{k}_j\mathbf{k}_k}$ $(i,j,k=1,2,3)$ describe all possible ways making the relevant terms to contribute along the direction $\mathbf{k}_{\mathbf{III}}=\mathbf{k}_1+\mathbf{k}_2-\mathbf{k}_3$. For example,

$$
\begin{aligned}
\mathcal{S}_{\mathbf{k}_3\mathbf{k}_2\mathbf{k}_1}(p_{lk}^{v'c':\mathbf{k}_3})^{*}p_{lj}^{v'c:\mathbf{k}_2}p_{ik}^{vc':\mathbf{k}_1} ={}& (p_{lk}^{v'c':\mathbf{k}_3})^{*}p_{lj}^{v'c:\mathbf{k}_2}p_{ik}^{vc':\mathbf{k}_1}+(p_{lk}^{v'c':\mathbf{k}_3})^{*}p_{lj}^{v'c:\mathbf{k}_1}p_{ik}^{vc':\mathbf{k}_2}+(p_{lk}^{v'c':-\mathbf{k}_2})^{*}p_{lj}^{v'c:-\mathbf{k}_3}p_{ik}^{vc':\mathbf{k}_1}\\
&+(p_{lk}^{v'c':-\mathbf{k}_2})^{*}p_{lj}^{v'c:\mathbf{k}_1}p_{ik}^{vc':-\mathbf{k}_3}+(p_{lk}^{v'c':-\mathbf{k}_1})^{*}p_{lj}^{v'c:-\mathbf{k}_3}p_{ik}^{vc':\mathbf{k}_2}+(p_{lk}^{v'c':-\mathbf{k}_1})^{*}p_{lj}^{v'c:\mathbf{k}_2}p_{ik}^{vc'-:\mathbf{k}_3}\\
={}& (p_{lk}^{v'c':\mathbf{k}_3})^{*}p_{lj}^{v'c:\mathbf{k}_2}p_{ik}^{vc':\mathbf{k}_1}+(p_{lk}^{v'c':\mathbf{k}_3})^{*}p_{lj}^{v'c:\mathbf{k}_1}p_{ik}^{vc':\mathbf{k}_2}+p_{lk}^{v'c':\mathbf{k}_2}(p_{lj}^{v'c:\mathbf{k}_3})^{*}p_{ik}^{vc':\mathbf{k}_1}\\
&+p_{lk}^{v'c':\mathbf{k}_2}p_{lj}^{v'c:\mathbf{k}_1}(p_{ik}^{vc':\mathbf{k}_3})^{*}+p_{lk}^{v'c':\mathbf{k}_1}(p_{lj}^{v'c:\mathbf{k}_3})^{*}p_{ik}^{vc':\mathbf{k}_2}+p_{lk}^{v'c':\mathbf{k}_1}p_{lj}^{v'c:\mathbf{k}_2}(p_{ik}^{vc':\mathbf{k}_3})^{*},
\end{aligned}
\tag{B2}
$$

where each density matrix has either positive or negative wave vector. Two other typical examples showing the operations of $\mathcal{S}_{\mathbf{k}_i\mathbf{k}_j}$ and $\mathcal{S}_{\mathbf{k}_i\mathbf{k}_j\mathbf{k}_k}$ are

$$
\begin{aligned}
&\mathbf{E}_2(t)\cdot\sum_{klv'c'}(\mu_{il}^{vc'})^{*}\mathcal{S}_{\mathbf{k}_3\mathbf{k}_1}(p_{kl}^{v'c':\mathbf{k}_3})^{*}p_{kj}^{v'c:\mathbf{k}_1}\\
&\quad=\mathbf{E}_2(t)\cdot\sum_{klv'c'}[(\mu_{il}^{vc'})^{*}(p_{kl}^{v'c':\mathbf{k}_3})^{*}p_{kj}^{v'c:\mathbf{k}_1}\\
&\qquad+(\mu_{il}^{vc'})^{*}(p_{kl}^{v'c':-\mathbf{k}_1})^{*}p_{kj}^{v'c:-\mathbf{k}_3}]\\
&\quad=\mathbf{E}_2(t)\cdot\sum_{klv'c'}[(\mu_{il}^{vc'})^{*}(p_{kl}^{v'c':\mathbf{k}_3})^{*}p_{kj}^{v'c:\mathbf{k}_1}\\
&\qquad+(\mu_{il}^{vc'})^{*}p_{kl}^{v'c':\mathbf{k}_1}(p_{kj}^{v'c:\mathbf{k}_3})^{*}]
\end{aligned}
\tag{B3}
$$

and

$$
\begin{aligned}
\mathcal{S}_{\mathbf{k}_3\mathbf{k}_2\mathbf{k}_1}(p_{lk}^{v'c':\mathbf{k}_3})^{*}B_{lkij}^{v'c'vc:\mathbf{k}_1+\mathbf{k}_2} ={}& (p_{lk}^{v'c':\mathbf{k}_3})^{*}B_{lkij}^{v'c'vc:\mathbf{k}_1+\mathbf{k}_2}\\
&+(p_{lk}^{v'c':-\mathbf{k}_2})^{*}B_{lkij}^{v'c'vc:\mathbf{k}_1-\mathbf{k}_3}\\
&+(p_{lk}^{v'c':-\mathbf{k}_1})^{*}B_{lkij}^{v'c'vc:\mathbf{k}_2-\mathbf{k}_3}\\
={}& (p_{lk}^{v'c':\mathbf{k}_3})^{*}B_{lkij}^{v'c'vc:\mathbf{k}_1+\mathbf{k}_2}\\
&+p_{lk}^{v'c':\mathbf{k}_2}B_{lkij}^{v'c'vc:\mathbf{k}_1-\mathbf{k}_3}\\
&+p_{lk}^{v'c':\mathbf{k}_1}B_{lkij}^{v'c'vc:\mathbf{k}_2-\mathbf{k}_3}.
\end{aligned}
\tag{B4}
$$

To solve Eq. (B1) for the time-dependent interband coherences matrix $p_{ij}^{vc:[\mathbf{k}_1+\mathbf{k}_2-\mathbf{k}_3]}$, we need the equations of motion for the first-order (in the optical field) density matrices $p_{ij}^{vc[\mathbf{k}_\alpha]}(\alpha=1,2,3)$; the three second-order two-exciton matrices $B_{lkij}^{v'c'vc:\mathbf{k}_1+\mathbf{k}_2}$, $B_{lkij}^{v'c'vc:\mathbf{k}_1-\mathbf{k}_3}$, and $B_{lkij}^{v'c'vc:\mathbf{k}_2-\mathbf{k}_3}$. The first-order equations are given by

$$
\begin{aligned}
-i\frac{\partial}{\partial t}p_{ij}^{vc[\mathbf{k}_\alpha]}-\frac{i}{\tau_{ex}}p_{ij}^{vc[\mathbf{k}_\alpha]} ={}& -\sum_n T_{jn}^{c}p_{in}^{vc[\mathbf{k}_\alpha]}-\sum_m T_{mi}^{v}p_{mj}^{vc[\mathbf{k}_\alpha]}\\
&+V_{ij}p_{ij}^{vc[\mathbf{k}_\alpha]}+\mathbf{E}_\alpha(t)\cdot(\mu_{ij}^{vc})^{*},\\
&(\alpha=1,2,3).
\end{aligned}
\tag{B5}
$$

The equations of motion for the three two-exciton density matrices are, respectively,

$$\begin{aligned}
&-i\frac{\partial}{\partial t}B_{lkij}^{v'c'vc:[\mathbf{k}_1+\mathbf{k}_2]}-\frac{i}{\tau_{2ex}}B_{lkij}^{v'c'vc:[\mathbf{k}_1+\mathbf{k}_2]}\\
&\quad=-\sum_m\{T_{jm}^{c}B_{lkim}^{v'c'vc:[\mathbf{k}_1+\mathbf{k}_2]}+T_{mi}^{v}B_{lkmj}^{v'c'vc:[\mathbf{k}_1+\mathbf{k}_2]}\\
&\qquad+T_{km}^{c}B_{lmij}^{v'c'vc:[\mathbf{k}_1+\mathbf{k}_2]}+T_{ml}^{v}B_{mkij}^{v'c'vc:[\mathbf{k}_1+\mathbf{k}_2]}\}\\
&\qquad+(V_{lk}+V_{lj}+V_{ik}+V_{ij}-V_{li}-V_{kj})B_{lkij}^{v'c'vc:[\mathbf{k}_1+\mathbf{k}_2]}\\
&\qquad-(V_{lk}+V_{ij}-V_{li}-V_{kj})\mathcal{S}_{\mathbf{k}_2\mathbf{k}_1}p_{ik}^{vc'[\mathbf{k}_1]}p_{lj}^{v'c[\mathbf{k}_2]}\\
&\qquad+(V_{ik}+V_{lj}-V_{li}-V_{kj})\mathcal{S}_{\mathbf{k}_2\mathbf{k}_1}p_{lk}^{v'c'[\mathbf{k}_1]}p_{ij}^{vc[\mathbf{k}_2]}, \qquad (B6)
\end{aligned}$$

$$\begin{aligned}
&-i\frac{\partial}{\partial t}B_{lkij}^{v'c'vc:[\mathbf{k}_1-\mathbf{k}_3]}-\frac{i}{\tau_{2ex}}B_{lkij}^{v'c'vc:[\mathbf{k}_1-\mathbf{k}_3]}\\
&\quad=-\sum_m\{T_{jm}^{c}B_{lkim}^{v'c'vc:[\mathbf{k}_1-\mathbf{k}_3]}+T_{mi}^{v}B_{lkmj}^{v'c'vc:[\mathbf{k}_1-\mathbf{k}_3]}\\
&\qquad+T_{km}^{c}B_{lmij}^{v'c'vc:[\mathbf{k}_1-\mathbf{k}_3]}+T_{ml}^{v}B_{mkij}^{v'c'vc:[\mathbf{k}_1-\mathbf{k}_3]}\}\\
&\qquad+(V_{lk}+V_{lj}+V_{ik}+V_{ij}-V_{li}-V_{kj})B_{lkij}^{v'c'vc:[\mathbf{k}_1-\mathbf{k}_3]}\\
&\qquad-(V_{lk}+V_{ij}-V_{li}-V_{kj})\mathcal{S}_{\mathbf{k}_1\mathbf{k}_3}p_{ik}^{vc'[\mathbf{k}_1]}(p_{lj}^{v'c[\mathbf{k}_3]})^*\\
&\qquad+(V_{ik}+V_{lj}-V_{li}-V_{kj})\mathcal{S}_{\mathbf{k}_1\mathbf{k}_3}p_{lk}^{v'c'[\mathbf{k}_1]}(p_{ij}^{vc[\mathbf{k}_3]})^*, \qquad (B7)
\end{aligned}$$

and

$$\begin{aligned}
&-i\frac{\partial}{\partial t}B_{lkij}^{v'c'vc:[\mathbf{k}_2-\mathbf{k}_3]}-\frac{i}{\tau_{2ex}}B_{lkij}^{v'c'vc:[\mathbf{k}_2-\mathbf{k}_3]}\\
&\quad=-\sum_m\{T_{jm}^{c}B_{lkim}^{v'c'vc:[\mathbf{k}_2-\mathbf{k}_3]}+T_{mi}^{v}B_{lkmj}^{v'c'vc:[\mathbf{k}_2-\mathbf{k}_3]}\\
&\qquad+T_{km}^{c}B_{lmij}^{v'c'vc:[\mathbf{k}_2-\mathbf{k}_3]}+T_{ml}^{v}B_{mkij}^{v'c'vc:[\mathbf{k}_2-\mathbf{k}_3]}\}\\
&\qquad+(V_{lk}+V_{lj}+V_{ik}+V_{ij}-V_{li}-V_{kj})B_{lkij}^{v'c'vc:[\mathbf{k}_2-\mathbf{k}_3]}\\
&\qquad-(V_{lk}+V_{ij}-V_{li}-V_{kj})\mathcal{S}_{\mathbf{k}_2\mathbf{k}_3}p_{ik}^{vc'[\mathbf{k}_2]}(p_{lj}^{v'c[\mathbf{k}_3]})^*\\
&\qquad+(V_{ik}+V_{lj}-V_{li}-V_{kj})\mathcal{S}_{\mathbf{k}_2\mathbf{k}_3}p_{lk}^{v'c'[\mathbf{k}_2]}(p_{ij}^{vc[\mathbf{k}_3]})^*, \qquad (B8)
\end{aligned}$$

where τ_{2ex} describes two-exciton dephasing times.

By solving Eqs. (B1) and (B5)–(B8), we obtain the $\mathbf{k}_{\mathbf{III}}$ component of interband coherences, $p_{ij}^{vc:[\mathbf{k}_1+\mathbf{k}_2-\mathbf{k}_3]}$. Then, $S_{\mathbf{III}}$ 2DCS can be obtained through Eq. (12). We found that for well separated pulses, numerical effort can be reduced significantly by employing only a subset of the above equations. Equations (B7) and (B8) can be neglected with small effects on the correlation energies. Therefore, all 2D spectra reported are calculated by neglecting Eqs. (B7) and (B8). This is equivalent to neglecting the $\mathcal{S}_{\mathbf{k}_3\mathbf{k}_2\mathbf{k}_1}$ before the term $(p_{lk}^{v'c':\mathbf{k}_3})^*B_{lkij}^{v'c'vc:\mathbf{k}_1+\mathbf{k}_2}$ in Eq. (B1), or including in Eq. (B4) only the term $B_{lkij}^{v'c'vc:\mathbf{k}_1+\mathbf{k}_2}$ but neglecting $B_{lkij}^{v'c'vc:\mathbf{k}_1-\mathbf{k}_3}$ and $B_{lkij}^{v'c'vc:\mathbf{k}_2-\mathbf{k}_3}$. This is also the general practice when calculating 2DCS for Frenkel excitons.

---

[1] H. Haug and S. W. Koch, *Quantum Theory of the Optical and Electronic Properties of Semiconductors*, 4th ed. (World Scientific, Singapore, 2004).

[2] J. Shah, *Ultrafast Spectroscopy of Semiconductors and Semiconductor Nanostructures*, 2nd ed. (Springer, New York, 1999).

[3] D. S. Chemla and J. Shah, Nature (London) **411**, 549 (2001).

[4] V. M. Axt and S. Mukamel, Rev. Mod. Phys. **70**, 145 (1998).

[5] F. Rossi and T. Kuhn, Rev. Mod. Phys. **74**, 895 (2002).

[6] K. Leo, M. Wegener, J. Shah, D. S. Chemla, E. O. Göbel, T. C. Damen, S. Schmitt-Rink, and W. Schäfer, Phys. Rev. Lett. **65**, 1340 (1990).

[7] M. Lindberg, Y. Z. Hu, R. Binder, and S. W. Koch, Phys. Rev. B **50**, 18060 (1994).

[8] N. H. Kwong and R. Binder, Phys. Rev. B **61**, 8341 (2000).

[9] W. Schäfer, D. S. Kim, J. Shah, T. C. Damen, J. E. Cunningham, K. W. Goossen, L. N. Pfeiffer, and K. Köhler, Phys. Rev. B **53**, 16429 (1996).

[10] Th. Östreich, K. Schönhammer, and L. J. Sham, Phys. Rev. Lett. **74**, 4698 (1995).

[11] G. Bartels, V. M. Axt, K. Victor, A. Stahl, P. Leisching, and K. Köhler, Phys. Rev. B **51**, 11217 (1995).

[12] T. Meier, S. W. Koch, M. Phillips, and H. Wang, Phys. Rev. B **62**, 12605 (2000).

[13] M. Hawton and M. M. Dignam, Phys. Rev. Lett. **91**, 267402 (2003).

[14] S. Mukamel, *Principles of Nonlinear Optical Spectroscopy* (Oxford University Press, New York, 1995).

[15] S. Mukamel, Annu. Rev. Phys. Chem. **51**, 691 (2000).

[16] Y. Tanimura and S. Mukamel, J. Chem. Phys. **99**, 9496 (1993).

[17] S. Mukamel and D. Abramavicius, Chem. Rev. (Washington, D.C.) **104**, 2073 (2004).

[18] J. Zheng, K. Kwak, J. Asbury, X. Chen, I. Piletic, and M. D. Fayer, Science **309**, 1338 (2005).

[19] Ch. Kolano, J. Helbing, M. Kozinski, W. Sander, and P. Hamm, Nature (London) **444**, 469 (2006).

[20] T. Brixner, J. Stenger, H. M. Vaswani, M. Cho, R. E. Blankenship, and G. R. Fleming, Nature (London) **434**, 625 (2005).

[21] M. C. Asplund, M. T. Zanni, and R. M. Hochstrasser, Proc. Natl. Acad. Sci. U.S.A. **97**, 8219 (2000).

[22] Xiaoqin Li, Tianhao Zhang, Camelia N. Borca, and Steven T. Cundiff, Phys. Rev. Lett. **96**, 057406 (2006).

[23] C. N. Borca, T. Zhang, X. Li, and S. T. Cundiff, Chem. Phys. Lett. **416**, 311 (2005).

[24] L. Yang, I. V. Schweigert, S. T. Cundiff, and S. Mukamel, Phys. Rev. B **75**, 125302 (2007).

[25] S. Mukamel, R. Oszwaldowski, and D. Abramavicius, Phys. Rev. B **75**, 245305 (2007).

[26] I. Kuznetsova, P. Thomas, T. Meier, T. Zhang, X. Li, R. P. Mirin, and S. T. Cundiff, Solid State Commun. **142**, 154 (2007).

[27] R. R. Ernst, G. Bodenhausen, and A. Wokaun, *Principles of Nuclear Magnetic Resonance in One and Two Dimensions* (Clarendon, Oxford, 1987).

[28] J. N. Evans, *Biomolecular NMR Spectroscopy* (Oxford University Press, New York 1995).

[29] H. P. Wagner, W. Langbein, and J. M. Hvam, Phys. Rev. B **59**, 4584 (1999).

[30] J. A. Leegwater and S. Mukamel, J. Chem. Phys. **101**, 7388 (1994).

[31] W. Zhuang, D. Abramavicius, and S. Mukamel, Proc. Natl. Acad. Sci. U.S.A. **102**, 7443 (2005).

[32] L. Yang and S. Mukamel, Phys. Rev. Lett. **100**, 057402 (2008).

[33] L. Bänyai, I. Galbraith, C. Ell, and H. Haug, Phys. Rev. B **36**, 6099 (1987).

[34] C. Sieh, T. Meier, F. Jahnke, A. Knorr, S. W. Koch, P. Brick, M. Hübner, C. Ell, J. Prineas, G. Khitrova, and H. M. Gibbs, Phys. Rev. Lett. **82**, 3112 (1999); C. Sieh, T. Meier, A. Knorr, F. Jahnke, P. Thomas, and S. W. Koch, Eur. Phys. J. B **11**, 407 (1999).

[35] A. Euteneuer, E. Finger, M. Hofmann, W. Stolz, T. Meier, P. Thomas, S. W. Koch, W. W. Rühle, R. Hey and K. Ploog, Phys. Rev. Lett. **83**, 2073 (1999).

[36] E. Finger, S. Kraft, M. Hofmann, T. Meier, S. W. Koch, W. Stolz, W. W. Rühle, and A. Wieck, Phys. Status Solidi B **234**, 424 (2002).

[37] S. Weiser, T. Meier, J. Möbius, A. Euteneuer, E. J. Mayer, W. Stolz, M. Hofmann, W. W. Rühle, P. Thomas, and S. W. Koch, Phys. Rev. B **61**, 13088 (2000).

[38] T. Meier, P. Thomas, and S. W. Koch, *Coherent Semiconductor Optics: From Basic Concepts to Nanostructure Applications* (Springer, New York, 2007).

[39] F. Meier and B. P. Zakharchenya, *Modern Problems in Condensed Matter Sciences* (North-Holland, Amsterdam, 1984), Vol. 8.

[40] K. Bott, O. Heller, D. Bennhardt, S. T. Cundiff, P. Thomas, E. J. Mayer, G. O. Smith, R. Eccleston, J. Kuhl, and K. Ploog, Phys. Rev. B **48**, 17418 (1993).

[41] T. Meier and S. Mukamel, Phys. Rev. Lett. **77**, 3471 (1996).

[42] H. Fukutome, J. Mol. Struct. **188**, 377 (1989), and references therein.

[43] F. C. Spano and S. Mukamel, Phys. Rev. Lett. **66**, 1197 (1991).

[44] J. A. Leegwater and S. Mukamel, Phys. Rev. A **46**, 452 (1992).

[45] V. M. Axt, and A. Stahl, Z. Phys. B: Condens. Matter **93**, 195 (1994).

[46] V. M. Axt and T. Kuhn, Rep. Prog. Phys. **67**, 433 (2004).

[47] J.-Y. Bigot, M.-A. Mycek, S. Weiss, R. G. Ulbrich, and D. S. Chemla, Phys. Rev. Lett. **70**, 3307 (1993).

[48] H. Wang, K. B. Ferrio, D. G. Steel, Y. Z. Hu, R. Binder, and S. W. Koch, Phys. Rev. Lett. **71**, 1261 (1993); H. Wang, K. B. Ferrio, D. G. Steel, P. R. Berman, Y. Z. Hu, R. Binder, and S. W. Koch, Phys. Rev. A **49**, R1551 (1994); Y. Z. Hu, R. Binder, S. W. Koch, S. T. Cundiff, H. Wang, and D. G. Steel, Phys. Rev. B **49**, 14382 (1994).

[49] S. W. Koch, C. Sieh, T. Meier, F. Jahnke, A. Knorr, P. Brick, M. Hübner, C. Ell, J. Prineas, G. Khitrova, and H. M. Gibbs, J. Lumin. **83-84**, 1 (1999).

[50] S. Tretiak, V. Chernyak, and S. Mukamel, Int. J. Quantum Chem. **70**, 711 (1998).